Cosmic tomography with weak gravitational lensing

Li, S.S.

CHAPTER 5

Weak lensing mass-luminosity scaling relations for galaxy groups: Testing the robustness of the halo model formalism

Abstract

Understanding the relation between baryonic observables and dark matter haloes is crucial for studying galaxy formation and evolution, and for deriving accurate cosmological constraints from galaxy surveys. In this chapter, we study this galaxy-halo connection by conducting a galaxy-galaxy weak lensing analysis on galaxy groups identified by the Galaxy and Mass Assembly survey, using galaxy shape catalogues from the fourth data release of the Kilo-Degree Survey. We interpreted the measured signals using a halo model formalism, employing a conditional luminosity function to describe the connection between halos and galaxies. Consistent with previous work, we found that the halo mass scales with the total r-band luminosity of the group according to a power law, with a slope of $1.25^{+0.12}_{-0.10}$. To assess the robustness of the current halo model formalism, we conducted sensitivity analyses. These revealed that the treatment of mis-centring in our model might introduce biases into the scaling relation constraints, which could exceed acceptable limits for future, more precise weak lensing measurements. To remedy this, it would be important to leverage insights from large-volume hydrodynamic simulations to develop a more physical model.

5.1 Introduction

According to the current standard model of cosmology, galaxies form within cold dark matter haloes, which originate from small initial density perturbations amplified by gravitational instability. This framework predicts a strong correlation between galaxy properties and the properties of their host dark matter haloes (see Wechsler & Tinker 2018, for a review). Dark matter haloes dominate the local gravitational potential, impacting matter clustering and providing the environment for the formation and evolution of galaxies (e.g. Blumenthal et al. 1984; Davis et al. 1985). On the flip side, various baryonic processes associated with galaxy formation, particularly the energetic feedback processes from supernovae (SNe) and active galactic nuclei (AGN), reshape the matter distribution on small scales (e.g. van Daalen et al. 2011; Hellwing et al. 2016; Chisari et al. 2018; van Daalen et al. 2020). Therefore, obtaining an accurate and precise understanding of the galaxy-halo connection is not only essential for studying galaxy formation and evolution, but also crucial for ensuring the accuracy of cosmological constraints derived from observations of large-scale structures (e.g. Semboloni et al. 2011; Schneider et al. 2020; Castro et al. 2021; Debackere et al. 2021).

Given that dark matter haloes typically host multiple galaxies, catalogues of galaxy groups and clusters are important in studying the galaxy-halo connection. Although massive galaxy clusters serve as a powerful tool for constraining cosmological models (see Allen et al. 2011, for a review), they are relatively rare and represent extreme conditions. On the other hand, galaxy groups, which host the majority of present-day galaxies and a significant portion of baryonic matter, offer a more representative view of galaxy formation (e.g. Robotham et al. 2011). They also contribute significantly to the cosmic shear signal (e.g. Semboloni et al. 2011; Debackere et al. 2020). Moreover, the gravitational binding energy of galaxy groups is comparable to the energy released by feedback processes from SNe and AGN, making galaxy groups particularly valuable for studying the impact of baryonic feedback (e.g. McCarthy et al. 2010; Kettula et al. 2015).

However, the robust identification of galaxy groups is a complex task that requires spectroscopic surveys with high spatial and redshift completeness. The Galaxy and Mass Assembly project (GAMA, Driver et al. 2011) represents one such effort. Achieving a 95 per cent spectroscopic completeness down to the r-band magnitude of 19.65 and covering approximately 250 deg^2 of sky area, GAMA currently offers the highest available redshift density over such an extensive area (Driver et al. 2022). As a result, it produced a reliable galaxy group catalogue with accurate estimations of group properties (Robotham et al. 2011).

The next challenge lies in measuring the dark matter properties of galaxy groups. This complexity becomes evident even when estimating basic properties like the mass of the dark matter haloes. For massive galaxy clusters, the X-ray measurement of the intracluster medium is commonly used for estimating the masses of individual clusters, under the assumption of hydrostatic equilibrium (see Ettori et al. 2013, for a review). However, when this method is applied to galaxy groups, its effectiveness diminishes

significantly due to their faint X-ray signals (e.g. Eckmiller et al. 2011; Pop et al. 2022; Bahar et al. 2022). Furthermore, various baryonic processes, including cooling, star formation, and feedback processes, can cause deviation from hydrostatic equilibrium, biasing the mass estimation that are based on this technique (e.g. Rasia et al. 2006; Biffi et al. 2016; Barnes et al. 2021; Logan et al. 2022).

Weak gravitational lensing provides an alternative approach to directly determining halo mass (e.g. Tyson et al. 1990; Hoekstra et al. 2001; Mandelbaum et al. 2006; Leauthaud et al. 2010; Hudson et al. 2015; Zacharegkas et al. 2022). It measures the subtle yet coherent distortions in the shapes of background galaxies, caused by the gravitational field of a foreground lens (see Bartelmann & Schneider 2001, for a review). These distortions directly trace the matter distributions in the foreground lenses, enabling the inference of total halo mass without requiring assumptions about their dynamical state.

However, the weak lensing signals produced by individual galaxy groups have low signal-to-noise ratios, which limits the precision of mass determinations for individual groups. To overcome this, we typically use an averaged measure from a collection of galaxy groups, which are selected and stacked based on narrowly binned observable properties. This method enables us to create a statistical description of the scaling relation between these observable properties and the masses of dark matter haloes (e.g. Viola et al. 2015; Rana et al. 2022).

To interpret stacked weak lensing measurements, we need a robust statistical model. The halo model combined with halo occupation statistics offers such a theoretical framework (e.g. Seljak 2000; Cooray & Sheth 2002; van den Bosch et al. 2013; Berlind & Weinberg 2002; Yang et al. 2003; Vale & Ostriker 2004; Cooray 2006). This approach statistically describes the properties of dark matter haloes and how galaxies inhabit them, thus creating a link between the underlying matter distributions and the statistical measures of weak lensing signals. In practice, the halo model contains several theoretically motivated or empirically required components, which are not always well constrained by the data. Combined with the intricate interplay and degeneracy among various parameters, this makes the selection of appropriate priors and interpretation of the parameters for the halo model a non-trivial task.

In this chapter, we study the scaling relation between group luminosity and halo mass, and assess the robustness of the current halo model formalism. We measure the weak lensing signals around galaxy groups identified by the GAMA survey, using the galaxy shape catalogue from the Kilo-Degree Survey (KiDS, de Jong et al. 2013; Kuijken et al. 2015). With the complete coverage of the three equatorial GAMA fields provided by the fourth data release of KiDS (KiDS-DR4, Kuijken et al. 2019; Giblin et al. 2021), our analysis has nearly double the sample volume compared to Viola et al. (2015). Moreover, we update the empirical modelling approach used by previous studies by adopting a more theoretically driven conditional luminosity function (e.g. Yang et al. 2003; Vale & Ostriker 2004; Cooray 2006). We evaluate the robustness of our current halo model framework by investigating its sensitivity to various adjustments in model setups. These sensitivity tests help identify crucial model ingredients and guide future

improvements. Considering the increased statistical power of the measured signals, such exploration and future enhancement of our current model are deemed necessary.

The rest of this chapter is structured as follows: Section 5.2 provides an overview of the data used in our analysis. Section 5.3 describes the measurements of weak lensing signals and the associated covariance matrix. The current modelling approach is introduced in Sect. 5.4, and the results derived from it are presented in Sect. 5.5. The sensitivity tests are discussed in Sect. 5.6. Finally, we conclude the chapter in Sect. 5.7. Throughout this chapter, we adopt a spatially flat Λ cold dark matter (ΛCDM) model, with parameters constrained by Planck Collaboration et al. (2020), for any calculations that require a cosmological framework: $\Omega_{\rm m} = 0.3158$, $\sigma_8 = 0.8120$, $n_{\rm s} = 0.96605$, $\Omega_{\rm b} = 0.04939$, and $h = 0.6732$. When we report values that are dependent on Hubble's constant, H_0, we include this dependency via $h = H_0/100$ km s^{-1} Mpc^{-1}, which facilitates comparison of results derived from different surveys and simulations.

5.2 Data

The data for our analysis originate from two surveys: the GAMA survey, which produced the galaxy group catalogue including baryonic observables such as stellar mass and luminosity; and the KiDS survey, which provided the shape measurements of background galaxies. In this section, we provide a concise overview of the catalogues used in our study. For further technical details, we direct interested readers to the relevant data release papers.

5.2.1 Lenses: GAMA groups

GAMA is a high-density, high-completeness spectroscopic survey conducted using the AAOmega instrument on the Anglo-Australian Telescope (Driver et al. 2011). Our analysis involves data from three equatorial fields of the GAMA II phase (G09, G12, G15), each covering a sky area of 60 square degrees (Liske et al. 2015). The GAMA data in these fields have a spectroscopic completeness of approximately 98 per cent for galaxies within the observed magnitude limit of $r < 19.8$. In particular, we use three key GAMA products: the G^{3}C group catalogue[1] (version 10, Robotham et al. 2011), the `StellarMassesLambdar` catalogue[2] (version 24, Taylor et al. 2011), and the random catalogue[3] (version 2, Farrow et al. 2015).

The G^{3}C group catalogue (version 10) consists of 26 194 groups identified using a friends-of-friends (FoF) algorithm. This method establishes connections between galaxies based on their three-dimensional separations. The algorithm has been validated on mock catalogues derived from semi-analytic simulations and has been found robust against outliers and linking errors. In our study, we only consider groups with a minimum of five identified members to reduce the impact of interlopers (Robotham et al. 2011).

[1] www.gama-survey.org/dr4/schema/dmu.php?id=115
[2] www.gama-survey.org/dr4/schema/dmu.php?id=1010
[3] www.gama-survey.org/dr4/schema/dmu.php?id=109

After applying this selection, we are left with a total of 2752 groups.

In our analysis, we consider the Brightest Cluster/group Galaxy (BCG) as the central galaxy. Another commonly used method for selecting the central galaxy involves iteratively removing group members that are furthest from the group's centre of light. However, Robotham et al. (2011) found that, for groups with more than five members, this iterative procedure converges on the BCG 95% of the time. For weak lensing analyses, the subtle difference between these two methods becomes even more statistically negligible, as illustrated in Appendix A of Viola et al. (2015).

The stellar masses of the BCGs are obtained from the `StellarMassesLambdar` catalogue (version 24). It estimates galaxy stellar masses using stellar population synthesis models from Bruzual & Charlot (2003), assuming a Chabrier (2003) initial mass function. The model fits are applied over a fixed rest-frame wavelength range (300 – 11000) using matched aperture photometry derived from the Lambda Adaptive Multi-Band Deblending Algorithm in R (LAMBDAR, Wright et al. 2016). We utilise the `logmstar` value from the catalogue, which represents the total mass of all luminous material and remnants, but excluding mass recycled back into the interstellar medium. We do not correct the aperture-photometry-based stellar mass, as the flux-based scaling factor has been removed from the latest GAMA stellar mass catalogue, and not all galaxies in the GAMA survey have an accurate total flux estimation.

The GAMA random catalogue (version 2) is employed in our analysis to quantify additive shear biases in the weak lensing signals. This catalogue comprises randomly distributed points, designed to reflect the same selection function as the main spectroscopic survey. For our analysis, we randomly select 1 million points from this catalogue for each of the GAMA fields under consideration. Since these random points do not correspond to any actual matter distribution in the field, performing equivalent weak lensing measurements around them illuminates potential systematic errors in our process.

5.2.2 Sources: KiDS galaxies

KiDS is a wide-field imaging survey, specifically designed to measure weak gravitational lensing effects (de Jong et al. 2013; Kuijken et al. 2015). It spans 1350 square degrees of the sky, with optical images in the $ugri$ bands taken from the ESO VLT Survey Telescope. Among these, the r-band images, offering the highest imaging quality, are used for measuring galaxy shapes. In collaboration with the VISTA Kilo-degree INfrared Galaxy survey (VIKING, Edge et al. 2013) using the nearby ESO VISTA telescope, the KiDS shear catalogue also incorporates photometry from five $ZYJHK_s$ near-infrared bands. This additional data significantly enhances the accuracy of photometric redshift estimates.

For our analysis, we employ the public KiDS-1000 shear catalogue from the fourth data release of KiDS (Kuijken et al. 2019; Giblin et al. 2021). This catalogue fully covers the three equatorial fields of GAMA, as illustrated in Fig. 5.1. Thanks to this complete coverage, we are now able to measure weak lensing signals around all 2752 selected GAMA groups, approximately doubling the number used in previous similar

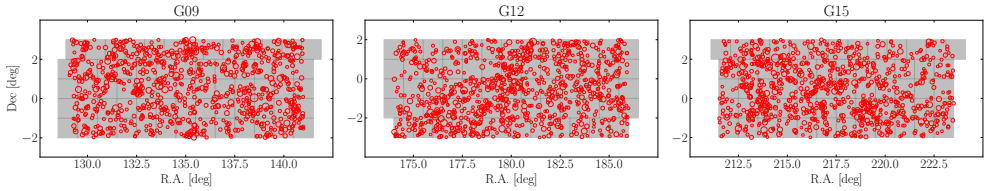

Figure 5.1: KiDS-DR4 coverage across the three equatorial GAMA fields (G09, G12, G15). The grey boxes represent KiDS tile images, each covering 1 square degree. The red circles indicate the selected GAMA groups, each consisting of at least five members. The size of these circles corresponds to the logarithm of the group richness. With the KiDS-DR4 data, we have achieved complete coverage of weak lensing measurements across the three equatorial GAMA fields.

analyses by Viola et al. (2015) and Rana et al. (2022).

The galaxy shapes in the KiDS-1000 catalogue are measured using the *lens*fit code (Miller et al. 2013; Fenech Conti et al. 2017) applied to the r-band images. These shear measurements are further calibrated using image simulations developed by Kannawadi et al. (2019). The photometric redshift estimates are derived from nine-band photometry using the BPZ code (Benítez 2000), and are calibrated with a spectroscopic reference sample as detailed in Hildebrandt et al. (2021).

5.3 Galaxy-galaxy weak lensing signals

The lensing effect introduces coherent tangential distortions in the apparent shapes of background galaxies. These distortions, known as the tangential shear, $\gamma_{\rm t}$, correlate with the projected mass density contrast of the foreground lens[4] (e.g. Bartelmann & Schneider 2001):

$$\Delta\Sigma(R) \equiv \bar{\Sigma}(\leq R) - \Sigma(R) = \Sigma_{\rm cr}\gamma_{\rm t}(R) \,, \tag{5.1}$$

where the mass contrast, $\Delta\Sigma(R)$, is also commonly referred to as the excess surface density (ESD). The $\Sigma(R)$ represents the local surface mass density at a projected comoving separation, R, between the lens and source, while $\bar{\Sigma}(\leq R)$ denotes the mean surface density within this radius. $\Sigma_{\rm cr}$, known as the critical surface density, serves as a measure of lensing efficiency and is defined as

$$\Sigma_{\rm cr} \equiv \frac{c^2}{4\pi G}\frac{D(z_{\rm s})}{D(z_{\rm l})D(z_{\rm l},\, z_{\rm s})} \,, \tag{5.2}$$

where G and c denote the gravitational constant and the speed of light, respectively. $D(z)$ is the angular diameter distance at redshift z.

[4]Throughout this work, we do not distinguish between the original shear γ and the reduced shear $g \equiv \gamma/(1-\kappa)$, given that the convergence κ is much less than one in the weak lensing regime.

Therefore, by measuring the ESD profile for foreground objects, we can infer their masses, assuming a certain density profile for the object. In this section, we detail how we estimate ESD for the selected GAMA galaxy groups from the KiDS shear measurements (Sect. 5.3.1) and the corresponding covariance matrix necessary for modelling (Sect. 5.3.2).

5.3.1 ESD measurements

We estimated the tangential shear by calculating the azimuthal average of the tangential projection, $\epsilon_{\rm t}$, of the *lens*fit measured ellipticities of the KiDS source galaxies. This is defined as

$$\begin{bmatrix} \epsilon_{\rm t} \\ \epsilon_{\times} \end{bmatrix} \equiv \begin{bmatrix} -\cos(2\phi) & -\sin(2\phi) \\ \sin(2\phi) & -\cos(2\phi) \end{bmatrix} \cdot \begin{bmatrix} \epsilon_1 \\ \epsilon_2 \end{bmatrix} , \tag{5.3}$$

where ϕ denotes the relative position angle of the source in relation to the lens. The azimuthal average of the cross projection, denoted as $\epsilon_{\times}$, can serve as a useful indicator of potential systematic contamination, given that the lensing effect only induces tangential shear to the leading order.

To account for both measurement and geometric effects, a weight was assigned to each lens-source pair during the computation of the azimuthal average. This weight is given by

$$w_{\rm ls} \equiv w_{\rm s}\, \tilde{\Sigma}_{\rm cr,l}^{-2} , \tag{5.4}$$

where $w_{\rm s}$ is the *lens*fit weight, which accounts for shape measurement uncertainties, and $\tilde{\Sigma}_{\rm cr,l}$ is the 'effective critical surface density'. The latter is used to down-weight lens-source pairs that are close in redshift and thus carry fewer lensing signals. This 'effective critical surface density' was calculated for each lens, by integrating the redshift distribution of the source galaxies behind the given lens to statistically represent the source distance. This approach is designed to mitigate the potential impact of uncertainties in the source redshift estimates. Following Eq. (5.2), the 'effective critical surface density' was calculated as

$$\tilde{\Sigma}_{\rm cr,l}^{-1} = \frac{4\pi G}{c^2} D(z_{\rm l}) \int_{z_{\rm l}+\delta_z}^{\infty} {\rm d}z_{\rm s}\, \frac{D(z_{\rm l},\, z_{\rm s})}{D(z_{\rm s})}\, n(z_{\rm s}) , \tag{5.5}$$

where the source redshift distribution $n(z_{\rm s})$ was determined from a deep spectroscopic reference catalogue that was re-weighted to closely match the KiDS-1000 sources (see Hildebrandt et al. 2021 for details). Following Dvornik et al. (2017), we introduced a redshift difference threshold, $\delta_z = 0.2$, to mitigate contamination from group members. This redshift cutoff, $z_{\rm s} > z_{\rm l} + \delta_z$, was applied to the source galaxies involved in the calculation as well as to the reference spectroscopic sample used for determining the source redshift distribution.

The median velocity dispersion of the GAMA galaxy groups used in our study is $\sim$300 km s^{-1}, which is not massive enough for measuring lensing signals from individual groups. Therefore, we used a stacking process to boost the signal-to-noise

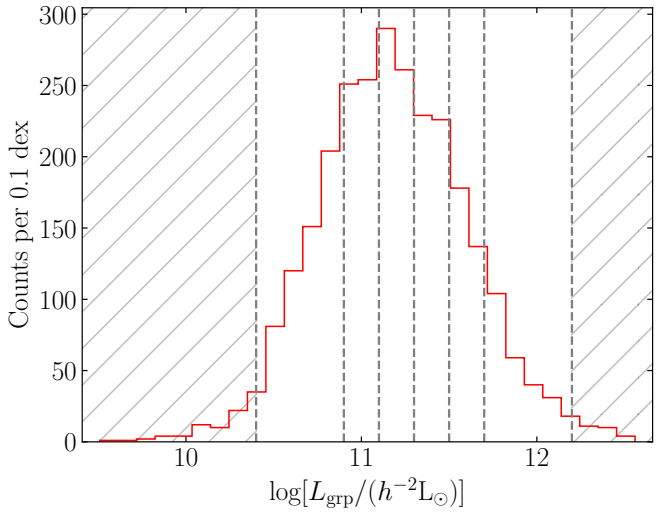

Figure 5.2: Distribution of the group total r-band luminosity underlying our binning strategy for the measurement of stacked ESD profiles. The vertical lines represent the boundaries of the bins, with their corresponding values detailed in Table 5.1. Objects falling within the hatched regions are excluded from our stacked analyses.

ratio. Following Eq. (5.1) and considering the weighting scheme mentioned above, the stacked ESD profile for an ensemble of galaxy groups can be estimated as

$$\Delta\Sigma(R) = \left[\frac{\sum_{\rm ls} w_{\rm ls}\, \epsilon_{\rm t}\, \tilde{\Sigma}_{\rm cr,l}}{\sum_{\rm ls} w_{\rm ls}}\right] \frac{1}{1+K}\,, \tag{5.6}$$

where the correction

$$K = \frac{\sum_{\rm ls} w_{\rm ls}\, m_{\rm s}}{\sum_{\rm ls} w_{\rm ls}}\,, \tag{5.7}$$

accounts for the multiplicative shear biases in the *lens*fit shape measurements. The correction factor was derived from image simulations developed by Kannawadi et al. (2019), who estimated an average m value for each redshift bin used in the KiDS-1000 cosmic shear analyses (Giblin et al. 2021; Asgari et al. 2021). We directly assigned these average m values to the galaxies used in our analysis based on their redshift, ignoring potential deviations in the galaxy size and signal-to-noise ratio distribution between the samples selected for our analysis and those used in the KiDS-1000 cosmic shear analyses. The overall correction factor is small, with K approximately equal to 0.001, and remains independent of the angular scale at which it is computed.

The additive shear biases were addressed by conducting weak lensing measurements around one million random points selected from the GAMA random catalogue (version 2, Farrow et al. 2015). These additive biases are both scale-dependent, with substantial biases on scales larger than $1h^{-1}$Mpc, and patch-dependent (see Appendix A of Dvornik

Table 5.1: Summary of the binning limits, number of groups, mean redshift of the groups, and the mean stellar mass of the BCGs for each bin used in the stacked ESD measurements.

Observable	Range	$N_{\rm groups}$	$z_{\rm mean}$	$M^{\rm BCG}_{\star,\rm mean}$
$L_{\rm grp}$	(10.4, 10.9]	628	0.12	10.59
	(10.9, 11.1]	477	0.17	10.79
	(11.1, 11.3]	528	0.21	10.91
	(11.3, 11.5]	432	0.26	11.00
	(11.5, 11.7]	312	0.29	11.08
	(11.7, 12.2]	267	0.32	11.18

The units for luminosity and stellar mass are given as $\log(L_{\rm grp}/[h^{-2}{\rm L}_\odot])$ and $\log(M_\star/[h^{-2}{\rm M}_\odot])$, respectively.

et al. 2017). Thus, we performed the correction separately for three GAMA patches (G9, G12, and G15). The overall corrections remain minor, with values at the sub-percent level, attributable to the complete coverage of the GAMA fields by the KiDS observations.

In our analysis, we divided the GAMA groups into six bins, based on their total r-band luminosity ($L_{\rm grp}$). We set lower and upper limits to exclude the tails of the distributions, as demonstrated in Fig. 5.2. This approach helps to mitigate group detection effects and prevents the estimates from being overly influenced by a small number of outliers within each bin. The boundaries for each bin were chosen to maintain similar signal-to-noise ratios across all bins in the measured ESDs. The statistical details of our defined bins are outlined in Table 5.1.

We measured the ESD profiles over 10 logarithmically-spaced radial bins, within a range of 0.03 to 2 h^{-1}Mpc. This range was determined by taking into account the signal-to-noise ratio at larger separations and the blending effects at smaller ones. The measured ESD profiles are illustrated in Fig. 5.3. The additive and multiplicative shear biases present in the original measurements were corrected using methods discussed earlier. The overall signal-to-noise ratios for the ESD measurements were found to be approximately 27.

5.3.2 Covariance matrix estimation

The ellipticity measurements of source galaxies can be used multiple times for $\Delta\Sigma(R)$ estimates across various radial bins and lenses, leading to correlations between the stacked ESD estimates. To account for these correlations in our modelling, we employed

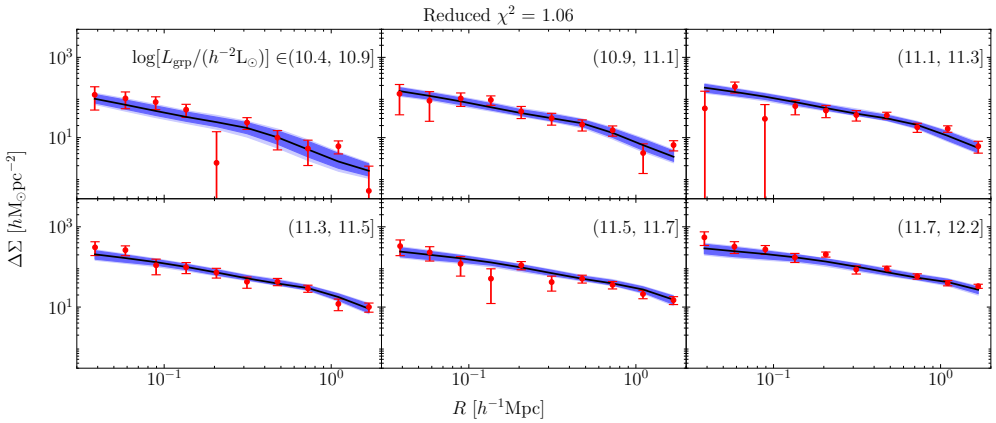

Figure 5.3: Excess Surface Density (ESD) profiles for selected GAMA groups, binned into six groups according to their total r-band luminosity ($L_{\rm grp}$). The error bars correspond to the square root of the covariance matrix's diagonal elements. The black lines depict the best-fit results obtained from our halo model, as detailed in Sect. 5.4. The dark and light blue shaded regions represent the 68% and 95% credible intervals of the fitting, respectively. The figure title shows the reduced χ^2 value of the best-fit results, calculated assuming 54 degrees of freedom (six independent fitting parameters to 60 data points).

the covariance matrix estimation technique as developed by Viola et al. (2015). This approach, proven valid in previous KiDS+GAMA analyses (e.g. Sifón et al. 2015; Brouwer et al. 2016), takes into account the shape noise of source galaxies and incorporates information about the survey geometry. However, it does not account for cosmic variance. Viola et al. (2015) demonstrated that this simplification is valid for measurements conducted within the range of $R \leq 2h^{-1}$Mpc, which is consistent with the range we adopt for our analysis.

5.4 Halo model and occupation statistics

From a statistical perspective, the projected mass surface density, $\Sigma(R)$, of an ensemble of lenses is related to the galaxy-matter cross-correlation function, $\xi_{\rm gm}(r)$, through the Abel transform:

$$\Sigma(R) = 2\,\bar{\rho}_{\rm m} \int_R^\infty {\rm d}r\ [\xi_{\rm gm}(r) + 1]\ \frac{r}{\sqrt{r^2 - R^2}}\,, \tag{5.8}$$

where we assume that the stacked density profile of the lenses is spherically symmetric. This is a valid assumption, given that our measurements are derived from stacking data from multiple lenses with varied orientations. Therefore, we can interpret the measured $\Delta\Sigma(R)$ signals if we have a model to describe $\xi_{\rm gm}(r)$. The halo model, complemented by halo occupation statistics, offers such a theoretical framework (e.g. Seljak 2000;

Cooray & Sheth 2002; Peacock & Smith 2000; Berlind & Weinberg 2002; Yang et al. 2003; van den Bosch et al. 2013).

In this section, we detail how we employ this framework to interpret our stacked ESD measurements. We begin with a concise overview of the halo model formalism in Sect. 5.4.1, largely adhering to the notations used by van den Bosch et al. (2013) and van Uitert et al. (2016). Then, we specify our choice of the model ingredients in Sect. 5.4.2. Our approach to halo occupation statistics is detailed in Sect. 5.4.3. Finally, we outline our fitting procedure in Sect. 5.4.4.

5.4.1 Halo model formalism

The halo model assumes that all dark matter resides within virialised haloes, the sizes of which are determined by a chosen overdensity threshold. In line with conventions in weak lensing studies, we define this threshold such that the average density within a certain radius is 200 times the mean density of the Universe, denoted as $\bar{\rho}_\mathrm{m}$. As a result, the mass of a specific halo can be formulated as

$$M_\mathrm{h} = \frac{4\pi}{3}\, 200\, \bar{\rho}_\mathrm{m}\, r_{200}^3 \,. \tag{5.9}$$

Using a formalism that encapsulates the internal density profile of these haloes, such as the widely used Navarro-Frenk-White (NFW) profile (Navarro et al. 1997), we can describe the matter-matter power spectrum of the Universe, using a theoretical approach based on the correlations between dark matter haloes (e.g. van den Bosch et al. 2013).

With a statistical understanding of how galaxies populate dark matter haloes, often referred to as halo occupation statistics, we can extend the halo model framework to include calculations for both the galaxy-galaxy power spectrum and the galaxy-matter power spectrum. Using the notation of van den Bosch et al. (2013) and van Uitert et al. (2016), we can concisely express the three types of power spectra as

$$P_{xy}(k) = P_{xy}^\mathrm{1h}(k) + P_{xy}^\mathrm{2h}(k) \,, \tag{5.10}$$

where

$$P_{xy}^\mathrm{1h}(k) = \int \mathrm{d}M_\mathrm{h}\, \mathcal{H}_x(k,\, M_\mathrm{h})\, \mathcal{H}_y(k,\, M_\mathrm{h})\, n_\mathrm{h}(M_\mathrm{h}) \,, \tag{5.11}$$

and

$$\begin{aligned} P_{xy}^\mathrm{2h}(k) = &\int \mathrm{d}M_{\mathrm{h},1}\, \mathcal{H}_x(k,\, M_{\mathrm{h},1})\, n_\mathrm{h}(M_{\mathrm{h},1}) \\ &\int \mathrm{d}M_{\mathrm{h},2}\, \mathcal{H}_y(k,\, M_{\mathrm{h},2})\, n_\mathrm{h}(M_{\mathrm{h},1})\, P_\mathrm{h}(k|M_{\mathrm{h},1}, M_{\mathrm{h},2}) \,. \end{aligned} \tag{5.12}$$

The terms $P_{xy}^\mathrm{1h}(k)$ and $P_{xy}^\mathrm{2h}(k)$, known as the one-halo and two-halo terms, describe the correlations within a single halo and between different haloes, respectively. Here, k represents the wavenumber, $n_\mathrm{h}(M_\mathrm{h})$ denotes the halo mass function, and $P_\mathrm{h}(k|M_{\mathrm{h},1}, M_{\mathrm{h},2})$

stands for the halo power spectrum associated with the mass values $M_{\rm h,1}$ and $M_{\rm h,2}$. This spectrum serves as a biased tracer of the linear dark matter power spectrum $P_{\rm m}^{\rm lin}(k)$:

$$P_{\rm h}(k|M_{\rm h,1}, M_{\rm h,2}) = b_{\rm h}(M_{\rm h,1})\ b_{\rm h}(M_{\rm h,2})\ P_{\rm m}^{\rm lin}(k)\ , \tag{5.13}$$

where $b_{\rm h}(M_{\rm h})$ refers to the large-scale halo bias. The subscripts, x and y, either refer to 'g' for galaxies or 'm' for matter, corresponding to different forms of $\mathcal{H}_x(k,\ M_{\rm h})$:

$$\mathcal{H}_{\rm m}(k,\ M_{\rm h}) \equiv \frac{M_{\rm h}}{\bar{\rho}_{\rm m}}\ \tilde{u}_{\rm m}(k|M_{\rm h})\ , \tag{5.14}$$

or

$$\mathcal{H}_{\rm g}(k,\ M_{\rm h}) \equiv \frac{\langle n_{\rm g}|M_{\rm h}\rangle}{\bar{n}_{\rm g}}\ \tilde{u}_{\rm g}(k|M_{\rm h})\ . \tag{5.15}$$

In these equations, $\tilde{u}_{\rm m}(k|M_{\rm h})$ describes the normalised density profile of dark matter haloes in Fourier space. The term $\tilde{u}_{\rm g}(k|M_{\rm h})$ describes the galaxy distributions within the halo, and its form depends on the types of galaxies. The term $\langle n_{\rm g}|M_{\rm h}\rangle$ refers to the average number of galaxies that reside in a halo of mass $M_{\rm h}$, i.e., the halo occupation distribution (HOD), and $\bar{n}_{\rm g}$ is the average number of galaxies integrated over all halo masses, given by

$$\bar{n}_{\rm g} = \int {\rm d}M_{\rm h}\ \langle n_{\rm g}|M_{\rm h}\rangle\ n_{\rm h}(M_{\rm h})\ . \tag{5.16}$$

The desired galaxy-matter cross-correlation function, $\xi_{\rm gm}$, is simply a Fourier transform of the galaxy-dark matter power spectrum $P_{\rm gm}(k)$:

$$\xi_{\rm gm}(r) = \frac{1}{2\pi^2}\int_0^\infty {\rm d}k\ P_{\rm gm}(k)\ \frac{\sin(kr)}{kr}\ k^2\ . \tag{5.17}$$

5.4.2 Model ingredients

For the internal density distribution of dark matter haloes, we adopted the Navarro-Frenk-White (NFW, Navarro et al. 1997) profile, with a mass-concentration relation from Duffy et al. (2008):

$$c_{\rm m} = f_{\rm c} \times 10.14\ \left(\frac{M_{\rm h}}{2\times10^{12}\ h^{-1}{\rm M}_\odot}\right)^{-0.081}\ (1+z_{\rm l})^{-1.01}\ , \tag{5.18}$$

where $f_{\rm c}$ is a scaling parameter, which we allowed to vary during the model fitting. The redshift dependence in this equation was derived from the results of a high-resolution N-body simulation conducted under the concordance ΛCDM cosmology (Bullock et al. 2001). Although more complex redshift dependencies are anticipated theoretically, they predominantly apply to redshifts greater than one (e.g. Muñoz-Cuartas et al. 2011), exceeding the highest lens redshift in our study.

To account for the mass contribution from central galaxies residing in the innermost region of the dark matter halo, we incorporated a point mass into the NFW density

profile. This mass was set to the mean stellar mass of the selected central galaxies for each stacked bin (see Table 5.1). Considering the scales of our ESD measurements, which range from 0.03 to 2 h^{-1}Mpc, our analysis is not sensitive to the detailed matter distributions within the innermost part of the dark matter halo.

For the halo mass function and the halo bias, we employed the calibrated fitting functions from Tinker et al. (2010), who derived parameters from a series of cosmological N-body simulations within the framework of the ΛCDM cosmology. Given that we fit the ESD profiles up to 2.0 h^{-1}Mpc, and that the halo bias only enters our calculations via the two-halo term (as shown in Eq. 5.12), our analysis is not sensitive to the precise form of the halo bias function given the current statistical uncertainties of the observed signals.

If the central galaxy (or in our case, the BCG) resides exactly at the centre of its host halo, the $\tilde{u}_{\rm g}(k|M_{\rm h})$ term shown in Eq. (5.15) would consistently equate to one. However, previous studies showed that BCGs often do not perfectly trace the centre of their host dark matter halos (e.g. Skibba et al. 2011; George et al. 2012; De Propris et al. 2021; Ahad et al. 2023). We statistically modelled this mis-centring following Viola et al. (2015) (also see Oguri & Takada 2011; More et al. 2015), with an equation:

$$\tilde{u}_{\rm g}(k|M_{\rm h}) = 1 - p_{\rm off} + p_{\rm off} \times \exp\left[-\frac{1}{2}\, k^2\, (r_{\rm s}\mathcal{R}_{\rm off})^2\right] , \tag{5.19}$$

where $r_{\rm s}$ represents the scale radius of the halo, as described by the NFW profile. This model assumes that a fraction $p_{\rm off}$ of BCGs is mis-centred, with the normalised radial distribution of these mis-centred galaxies relative to the true halo centre following a Gaussian distribution with a width of $r_{\rm s}\mathcal{R}_{\rm off}$. It is clear that setting either $p_{\rm off}$ or $\mathcal{R}_{\rm off}$ to zero results in a model without mis-centring. In our current fiducial model, we treated both $p_{\rm off}$ and $\mathcal{R}_{\rm off}$ as uninformative free parameters.

Although the incorporation of these two mis-centring parameters seems physically well-motivated, the data might not fully comply with the idealised assumptions of this model, which imply an isotropic random mis-identification of group centres leading to a Gaussian radial distribution of mis-centred galaxies, and also presume perfect group identification. For example, Ahad et al. (2023) found that line-of-sight projections, which result in a discrepancy between the projected and intrinsic luminosity, account for approximately half of the identified mis-centred groups in their simulations. Furthermore, the GAMA group-finding algorithm is susceptible to aggregation and fragmentation effects (see Appendix A of Jakobs et al. 2018). Aggregation refers to the phenomenon where two smaller groups, located in close proximity and linked by an intermediate galaxy, are identified as a single larger group. On the other hand, fragmentation occurs when a single, intrinsically large group is identified as several smaller groups. According to Ahad et al. (2023), the aggregation effects cause mis-centring in roughly 5% of their sample. Further complicating the issue is the high degeneracy observed between the mis-centring parameters and the concentration scaling parameter, $f_{\rm c}$ (see Sect. 5.1.2 of Viola et al. 2015). All these factors make the practical handling and interpretation of the mis-centring parameters challenging. We assess the robustness of the constrained halo

masses against various setups of mis-centring parameters to guide future improvements, in Sect. 5.6.

5.4.3 Halo occupation statistics

To extend the halo model framework for interpreting the galaxy-matter power spectrum used in the analysis of measured ESD signals (Eqs. 5.8 and 5.17), we require a formalism to describe the term $\langle n_{\rm g}|M_{\rm h}\rangle$ in Eq. (5.15). This term, often referred to as the halo occupation statistics or the halo occupation distribution (HOD), can be addressed in two ways. One approach involves directly constructing models to represent the average number of galaxies or groups associated with a dark matter halo of mass $M_{\rm h}$ (e.g. Berlind & Weinberg 2002). Alternatively, we can use the conditional stellar mass or luminosity function (CLF) to express the number density of galaxies or groups, based on their stellar mass or luminosity, given a halo mass (e.g. Yang et al. 2003). In our analysis, we opt for the latter methodology due to its direct connection to the relation between baryonic observable properties and halo mass, which is the focus of our study. It is worth noting that our CLF-based HOD model differs from the previous analysis by Viola et al. (2015), who defined the HOD directly based on the average number of groups as a function of halo mass.

In our fiducial model, we adopted a log-normal distribution to describe the group luminosity distribution given a halo mass. This has proven to be a validated CLF for central galaxy properties (e.g. Yang et al. 2008; Cacciato et al. 2009; van den Bosch et al. 2013; van Uitert et al. 2016):

$$\Phi(L_{\rm grp}|M_{\rm h}) = \frac{1}{\sqrt{2\pi}\,\ln(10)\,\sigma_L\,L_{\rm grp}}\,\exp\left[-\frac{(\log L_{\rm grp}-\log L_{\rm grp,m})^2}{2\sigma_L^2}\right]. \tag{5.20}$$

This function consists of two free parameters: the scatter σ_L and the mean $L_{\rm grp,m}$ for a given halo mass $M_{\rm h}$. In our current model, we considered σ_L as a halo mass-independent free parameter, following van Uitert et al. (2016). For the mean $L_{\rm grp,m}$, we assumed a power-law scaling relation between $L_{\rm grp,m}$ and the halo mass $M_{\rm h}$:

$$\frac{L_{\rm grp,m}}{10^{11.5}\,h^{-2}{\rm L}_\odot} = C_L\,\left(\frac{M_{\rm h}}{10^{14}\,h^{-1}{\rm M}_\odot}\right)^{\alpha_L}, \tag{5.21}$$

where C_L denotes the amplitude and α_L is the index. Both are free parameters in our fitting process.

Under the assumption of sample completeness, which is valid given the high completeness of the GAMA survey and our exclusion of distribution tails (see Fig. 5.2), we can calculate the mean number of groups per specific observable bin as follows:

$$\langle n_{\rm g}|M_{\rm h}\rangle = \int_{L_{\rm grp,min}}^{L_{\rm grp,max}} {\rm d}L_{\rm grp}\,\Phi(L_{\rm grp}|M_{\rm h})\,, \tag{5.22}$$

Table 5.2: Free parameters in our fiducial model, including their priors and derived constraints.

Parameter	Prior	Constraints
f_c	[0.2, 3]	$1.23^{+0.30}_{-0.26}$
p_{off}	[0, 1]	$0.50^{+0.08}_{-0.10}$
$\mathcal{R}_{off}$	[0, 3.5]	$3.13^{+0.27}_{-0.48}$
σ_L	[0.01, 2]	$0.07^{+0.07}_{-0.05}$
C_L	[0, 3]	$0.98^{+0.12}_{-0.14}$
α_L	[0, 5]	$0.80^{+0.07}_{-0.07}$

The parameters can be categorised into two main groups. The first group contains the standard halo model components (Sect. 5.4.2), while the second group includes parameters associated with the halo occupation statistics (Sect. 5.4.3). The reported constraints correspond to the marginalised median values of the sampling, with the uncertainties indicating the marginalised 68% credible intervals.

where $L_{grp,min}$ and $L_{grp,max}$ denote the lower and upper boundaries of the binning, respectively, as detailed in Table 5.1. We assess the impact of potential sample incompleteness in Sect. 5.6.

5.4.4 Model fitting

We fitted the aforementioned halo model to the stacked ESD measurements and sampled the posterior space using the `emcee` code (Foreman-Mackey et al. 2013), which implements the affine invariant Markov Chain Monte Carlo (MCMC) ensemble sampler (Goodman & Weare 2010). The convergence of the MCMC chains is evaluated using the integrated autocorrelation time (e.g. Goodman & Weare 2010). For the halo model calculations requiring lens redshifts, we used the mean redshifts from each stacked bin, as presented in Table 5.1. Our fiducial model incorporates six free parameters, all assigned broad, uninformative priors. The ranges for these priors are detailed in Table 5.2.

5.5 Results from the fiducial model

The best-fit results for the ESD profiles, along with their 68% and 95% credible intervals, are illustrated in Fig. 5.3. The reduced best-fit χ^2 value for our current fiducial model is approximately 1.06, assuming independence among the six free parameters in the model. This suggests a reasonable fit of our fiducial model to the data. The constraints

on the model parameters are presented in Table 5.2 as median values derived from the marginalised distributions, accompanied by their uncertainties representing the 68% credible intervals. The corresponding posterior distributions of these parameters are visualised as contour plots in Appendix 5.A.

5.5.1 Stacked halo masses

While our CLF-based halo model offers a direct estimation of the scaling relation between stacked properties and halo mass, via Eq. (5.21), it is instructive to estimate the average halo mass $\langle M_\mathrm{h} \rangle$ for each stacked bin. We can calculate this using the following equation:

$$\langle M_\mathrm{h} \rangle = \int \mathrm{d}M_\mathrm{h}\, \mathcal{P}(M_\mathrm{h}) M_\mathrm{h} \,, \tag{5.23}$$

where

$$\mathcal{P}(M_\mathrm{h}) = \int_{L_\mathrm{grp,min}}^{L_\mathrm{grp,max}} \mathrm{d}L_\mathrm{grp}\, \mathcal{P}(M_\mathrm{h}|L_\mathrm{grp}) \,, \tag{5.24}$$

is an integral of the conditional halo mass distribution $\mathcal{P}(M_\mathrm{h}|L_\mathrm{grp})$ for a given observable value of L_grp, which can be derived from the components of the halo model using Bayes' theorem:

$$\mathcal{P}(M_\mathrm{h}|L_\mathrm{grp}) = \frac{\Phi(L_\mathrm{grp}|M_\mathrm{h})\; n_\mathrm{h}(M_\mathrm{h})}{\bar{n}_\mathrm{g}} \,, \tag{5.25}$$

where $\Phi(L_\mathrm{grp}|M_\mathrm{h})$ is the CLF presented in Eq. (5.20), n_h is the halo mass function from Tinker et al. (2010), and $\bar{n}_\mathrm{g}$ is the average number of galaxies, as defined in Eq. (5.16).

Figure 5.4 shows the inferred halo mass distributions and the corresponding average halo mass for each stacked bin. To demonstrate the scatter in the sampled halo mass distributions, we randomly selected 100 sets of model parameter values from the sample space and plotted the corresponding distributions. The vertical lines in the figure represent the median values of the estimated average halo masses, with the shaded regions indicating the 68% credible intervals. Most of the sampled distributions exhibit well-defined peaks around the median values of the estimated average halo masses. As we move towards bins with higher observable values, the overall distribution shifts towards larger halo mass values. This scaling relation is quantified by the two parameters presented in the power-law scaling function of Eq. (5.21).

5.5.2 Group luminosity-halo mass relation

One key advantage of our CLF-based halo mass model, in contrast to the model employed by Viola et al. (2015), is its ability to directly constrain the scaling relation between the stacked properties and halo mass during the main sampling procedure. Given that the scaling relation is a part of our CLF-based model (Eq. 5.21), it obviates the need for an additional linear regression process performed on the estimated mean halo masses and stacked observable values, which can be challenging due to correlated measurement errors and intrinsic scatter in these averaged properties (e.g. Kelly 2007).

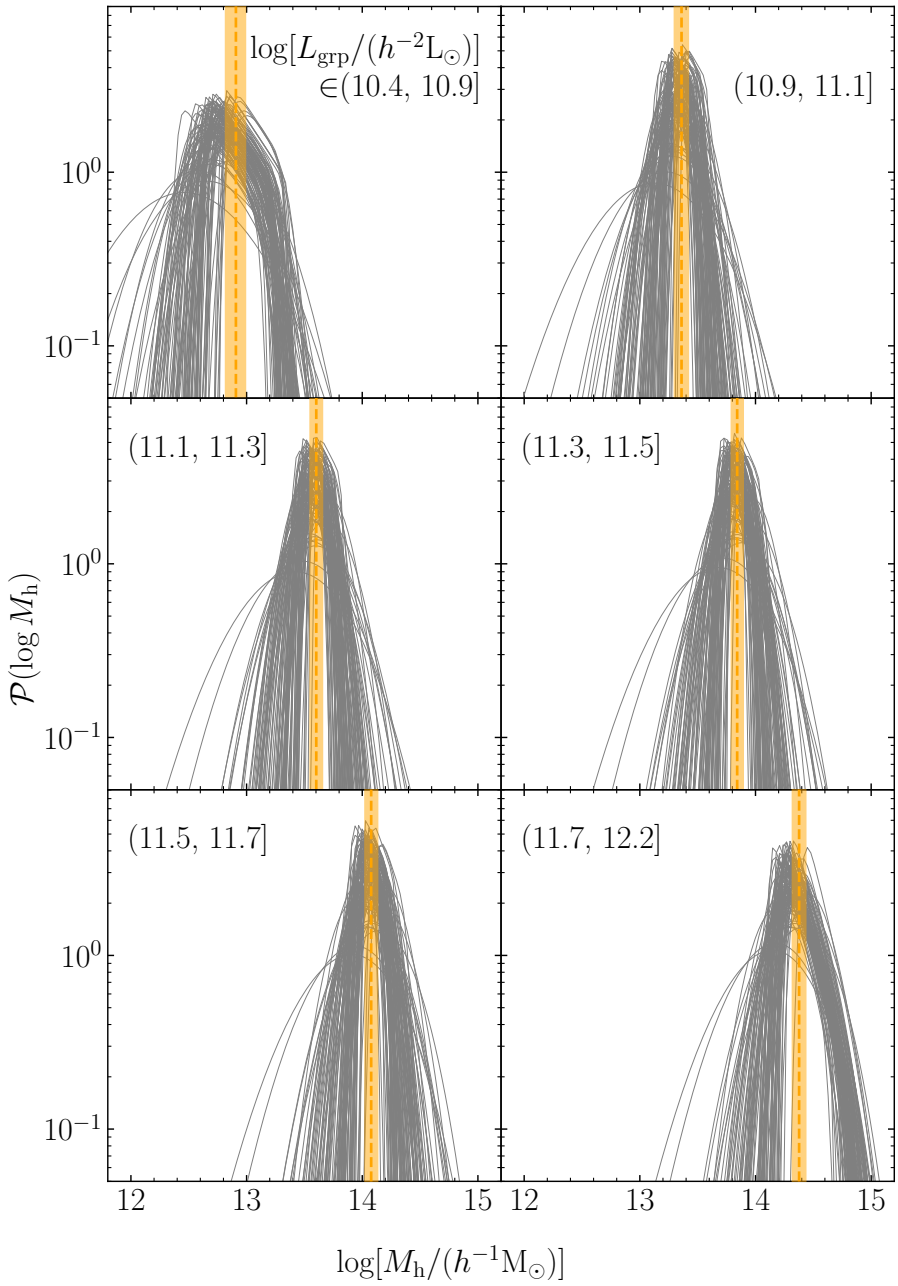

Figure 5.4: Halo mass distributions and average halo masses for each stacked bin. Grey lines illustrate the distributions derived from 100 randomly selected sets of parameter values from the sampling. Orange dashed vertical lines denote the median values of the estimated average halo masses, and the shaded regions represent the corresponding 68% credible intervals. These average halo masses were calculated from the sampled halo mass distributions, according to Eq. (5.23).

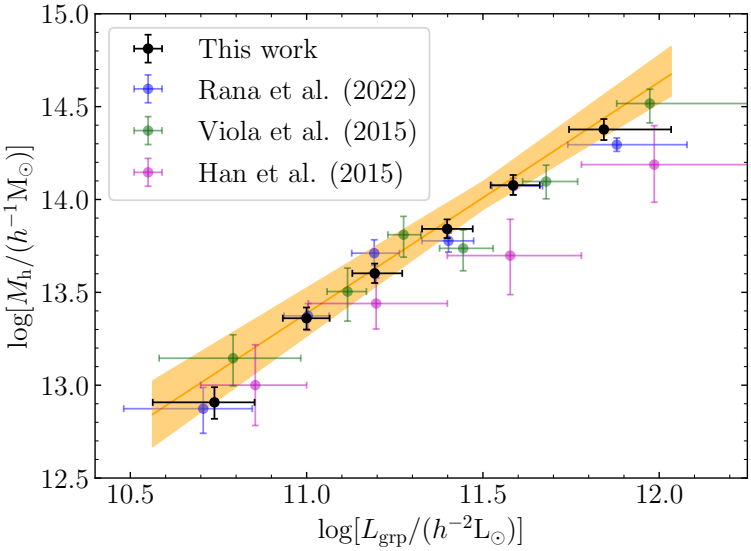

Figure 5.5: Relation between the r-band luminosity of galaxy groups and their halo masses, as determined from our weak lensing analysis. The orange line represents results derived from the median values of the estimated parameters, with the shaded regions illustrating the corresponding 68% credible intervals; the parameter values are provided in Table 5.2. The black points represent the average halo masses calculated in Sect. 5.5.1, with the error bars denoting the 68% credible intervals. The corresponding L_{grp} values for these points are derived as the median values of each stacked bin, with error bars denoting the 16th and 84th percentiles of the distribution within the bin. Results from previous weak lensing analyses based on HSC data (Rana et al. 2022), the first KiDS weak lensing data (Viola et al. 2015), and SDSS data (Han et al. 2015) are represented by blue, green, and magenta points, respectively. We note that our scaling relation is directly extracted from our CLF-based halo model, rather than fitted the estimated mean halo mass values, so the orange line is not expected to align perfectly with the black points, due to different marginalisations of the high-dimensional parameter space.

Figure 5.5 presents the scaling relation between the r-band luminosity of galaxy groups and their halo masses, as estimated from our current halo model. It also compares these results with mean halo masses estimated in Sect. 5.5.1 and from previous weak lensing analyses of the GAMA group sample, albeit with different source samples. These analyses include recent studies based on weak lensing measurements from the Subaru Hyper Suprime-Cam (HSC) survey (Rana et al. 2022), the first KiDS weak lensing data (Viola et al. 2015), and the Sloan Digital Sky Survey (SDSS, Han et al. 2015). Considering the differences in data sets and modelling procedures, the remarkable consistency between the various analyses confirms the overall validity of our new CLF-based halo model for galaxy group studies.

5.6 Model sensitivity analyses

While our current halo model generally offers a good fit to the data, as evidenced by a reduced χ^2 value of 1.06 for the best-fit model, the physical interpretation of the constrained parameters can be complex. This complexity arises primarily from the idealised assumptions inherent in our model, which may not always align with the realities of the data, particularly given the complexity of the group-finding procedure not accounted for in our current idealised model. Furthermore, the degeneracy among model parameters could introduce bias into the estimation of certain parameters when derived from projected marginalisations. These factors complicate the interpretation of our estimated model parameters and prompt questions about the robustness of our scaling relation estimates. Acknowledging these challenges, we perform sensitivity analyses in this section, focusing on two key areas of uncertainty: selection effects (Sect. 5.6.1) and mis-centring parameters (Sect. 5.6.2). These tests serve to assess not only the robustness of our current model but also to provide valuable insights for potential improvements in our future modelling efforts.

5.6.1 Sensitivity to the incompleteness

An important assumption in our CLF-based halo model is that the analysed sample is complete, implying that every halo with a specific halo mass M_h has a detected central galaxy. This assumption facilitates the integration of Eq. (5.22) to estimate the average number of galaxies for a given halo mass. Even though this is a reasonable assumption for the highly complete GAMA sample, it is worth investigating potential sample incompleteness. To address this, we introduced an incompleteness function into the integration to account for cases where certain haloes might not include a detected central galaxy:

$$\langle n_\mathrm{g}|M_\mathrm{h}\rangle = \int_{L_\mathrm{grp,min}}^{L_\mathrm{grp,max}} \mathrm{d}L_\mathrm{grp}\ \Phi(L_\mathrm{grp}|M_\mathrm{h})\ F_\mathrm{I}(M_\mathrm{h})\ , \tag{5.26}$$

where the incompleteness function $F_\mathrm{I}(M_\mathrm{h})$ is defined as:

$$F_\mathrm{I}(M_\mathrm{h}) \equiv \frac{1}{2}\left[1+\mathrm{erf}\left(\frac{\log M_\mathrm{h}-\log M_\mathrm{erf}}{\sigma_\mathrm{erf}}\right)\right]\ , \tag{5.27}$$

with $\mathrm{erf}(M_\mathrm{h})$ being an error function with a characteristic mass of M_erf and scatter σ_erf. This incompleteness model assumes that the sample incompleteness increases or decreases monotonically with respect to the halo mass, an approach similar to those used by van Uitert et al. (2016) and Tinker et al. (2013).

This test model comprises eight free parameters. Assuming parameter independence, we obtained a reduced χ^2 value of 1.04, which marginally surpasses the 1.06 derived from our fiducial six-parameter model. Upon visualising the fitted ESD profiles, we observed that most improvements occurred in the lowest luminosity bin, which is

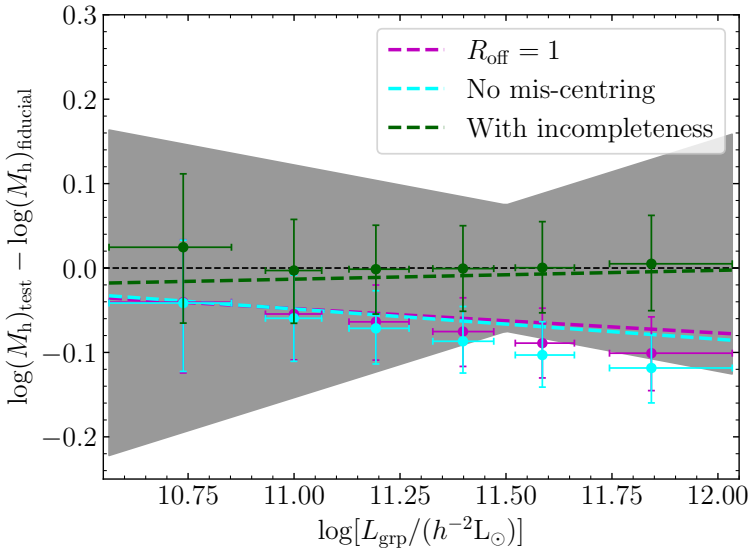

Figure 5.6: Shifts in the constrained average halo masses and scaling relation resulting from our sensitivity analyses concerning sample incompleteness and mis-centring. The shaded regions represent the 68% credible regions of the fiducial model's constraints on the scaling relation between the halo mass and group r-band luminosity. The points indicate the shifts in the constrained average halo masses, while the lines denote the shifts in the constrained scaling relations. The colour green corresponds to results from the incompleteness test (Sect. 5.6.1), whereas magenta and cyan represent results from the two mis-centring-related test models (Sect. 5.6.2). Results from the test model with fixed $p_{\rm off} = 1$ are not shown due to the lack of convergence.

expected for a flux-limited survey. However, when examining the posterior distributions, we found that the two incompleteness parameters are not constrained by the current data. Furthermore, the average halo mass estimation and the scaling relation inferred from this more complicated model closely align with the results from the fiducial model, as illustrated in Fig. 5.6. Following the principle of Occam's Razor, we conclude that introducing two more incompleteness parameters into our current model is not necessary.

5.6.2 Sensitivity to the mis-centring parameters

As previously noted in Sect. 5.4.2, the causes of mis-centring in a group sample are more intricate than what the idealised Gaussian distribution-based mis-centring model accounts for. The simplicity of our model complicates the interpretation of the estimated mis-centring parameters. This complication is further exacerbated by their degeneracy with the concentration parameter, as demonstrated in the projected contour plot of Fig. 5.7. Moreover, the posterior distribution of $\mathcal{R}_{\rm off}$ shows a tendency to lean towards the higher

limit of our already broad priors, suggesting that the simple Gaussian distribution model has difficulty describing the complex mis-centring in our data. This raises questions regarding its effect on our halo mass estimates and scaling relation constraints.

Therefore, we performed sensitivity analyses by varying the configurations of the mis-centring parameters within the framework of the current model. The exploration of more realistic mis-centring models will be left to our future analyses. We tested three alternate setups of the mis-centring parameters: fixing $p_{\rm off} = 1$ and only varying $\mathcal{R}_{\rm off}$ to examine if a single Gaussian distribution suffices for describing the central galaxy position distribution of the entire sample; fixing $\mathcal{R}_{\rm off} = 1$ and only varying $p_{\rm off}$ to explore if altering the mis-centred fraction alone can adequately describe the mis-centring scenario; and setting both $p_{\rm off}$ and $\mathcal{R}_{\rm off}$ to zero to ascertain whether the mis-centring effect can be ignored in the current analysis.

We first checked the posterior distributions of test runs and compared them to those from the fiducial model, as shown in Fig. 5.7. Except for the case where we fix $p_{\rm off} = 1$, the other two alternatives yield well-constrained model parameters. The lack of convergence in the case with fixed $p_{\rm off} = 1$ indicates that a single Gaussian distribution fails to describe the central galaxy position distribution of the entire sample, suggesting that most central galaxies remain close to the group's true centre and thus follow a much sharper distribution. We also found that changes in the mis-centring parameters affect the constraints on the concentration parameter $f_{\rm c}$ due to their degeneracy. Specifically, downplaying or disregarding mis-centring effects drives $f_{\rm c}$ towards lower values, warranting caution in interpreting the concentration parameter constrained in the current model, a finding consistent with Viola et al. (2015).

Next, we examined the fitted ESD profiles and the best-fit χ^2 values. The test models yielded slightly sub-optimal fits, with reduced χ^2 values of 1.34 and 1.35 for the cases with $\mathcal{R}_{\rm off} = 1$ and without mis-centring, respectively. Upon visually inspecting the fitted ESD profiles, we found that the noticeable degradation in fit occurs in the small separation measurements in the higher $L_{\rm grp}$ bins. These results imply that a model lacking proper consideration for the mis-centring of selected central galaxies would struggle to accurately describe the innermost regions of the measured ESD signals.

Finally, we investigated the impact of these test models on the estimations of average halo mass and scaling relations. As illustrated in Fig. 5.6, alterations in the setups of the mis-centring parameters affect both constraints, particularly at the high mass end. Interestingly, the scaling relation, directly constrained by our CLF-based halo model, demonstrates a greater robustness against changes in the mis-centring parameters. The most significant shift remains within the 68% credible regions of the fiducial constraints. In contrast, the average halo mass exhibits shifts that slightly exceed the 68% credible regions of the fiducial constraints. This outcome lends additional credence to our approach of directly constraining the scaling relations from the model, as opposed to fitting them to the measured average values.

These tests, which focus on the mis-centring parameters, underscore the importance of properly accounting for mis-centring within the group sample. Our current fiducial model appears to outperform all test models due to its better fit to the measured signals.

However, the impact on the scaling relation constraints from these model variations is concerning for upcoming, more precise measurements, and underscores the need for the development of a more sophisticated mis-centring model. We plan to address this in our future analyses, using hydrodynamic simulations as a tool for model refinement.

5.7 Conclusions

We conducted a galaxy-galaxy weak lensing analysis using the KiDS-1000 data, aiming to constrain the scaling relation between the group luminosity and their halo masses for galaxy groups identified by GAMA. The size of our sample is nearly double of that used in the similar work conducted by Viola et al. (2015). Furthermore, we updated their empirical Halo Occupation Distribution (HOD) model with a more physically motivated Conditional Luminosity Function (CLF, Yang et al. 2003; Vale & Ostriker 2004; Cooray 2006). Our new CLF-based halo model incorporates six free parameters, compared to the eleven free parameters in the previous model. Most importantly, it allows for direct sampling of the scaling relation parameters during the main modelling procedure, thereby bypassing the need for an additional regression process based on the average halo mass estimates as required in previous studies. Despite having considerably fewer free parameters, our current model still provides a good fit to the Excess Surface Density (ESD) measurements, with a best-fit reduced χ^2 value of 1.06.

Our current fiducial model yields a power-law relation between the halo mass and the r-band luminosity of the group:

$$\frac{M_\mathrm{h}}{10^{14}\ h^{-1}\mathrm{M}_\odot} = \left(1.02^{+0.22}_{-0.14}\right)\left(\frac{L_\mathrm{grp}}{10^{11.5}\ h^{-2}\mathrm{L}_\odot}\right)^{1.25^{+0.12}_{-0.10}} . \tag{5.28}$$

These results align with previous findings from Viola et al. (2015), who reported a normalisation of 0.95 ± 0.14 and a power-law index of 1.16 ± 0.13, and Rana et al. (2022), who reported a normalisation of 0.81 ± 0.04 and a power-law index of 1.01 ± 0.07.

While our overall sample size is larger than that used by Viola et al. (2015), the uncertainties of our final constraints are comparable to theirs. This is largely because we applied a more stringent scale cut to alleviate blending effects on small scales—we used a scale cut of 0.03 h^{-1}Mpc compared to their 0.02 h^{-1}Mpc. Additionally, we excluded the tails of the L_grp distributions to mitigate potential group detection effects, as shown in Fig. 5.2. In this sense, we consciously traded some statistical power for increased robustness. Crucially, our sensitivity tests revealed that uncertainties in certain elements of our current halo model do have an impact on our results, although the impact is within acceptable limits given the current measurement uncertainties. This underscores the necessity for further model refinement to prepare for future analyses with more precise measurements.

Most importantly, we acknowledge the limitations of the current model in accurately representing the innermost regions of the ESD measurements. These small-scale measurements exhibit strong sensitivity to both the mass-concentration and mis-centring

parameters. Moreover, these parameters display similar impacts on the measured ESD signals, leading to a degeneracy between them in the current model, a finding also reported by Viola et al. (2015). Our sensitivity tests further revealed that alterations to the configuration of the mis-centring parameters can impact the constraints on the scaling relation to a degree that is only marginally acceptable for the current analysis. Given the complex origins of mis-centring in a galaxy group sample, as noted in Sect. 5.4.2 and also in Ahad et al. (2023) and Jakobs et al. (2018), we believe the development of a more realistic mis-centring model is one of the crucial aspects for future analyses.

Such advancement can be achieved through the analysis of galaxy-galaxy lensing measurements and modelling within the context of cosmological simulations. With the advent of new large-volume hydrodynamic simulations (e.g. Schaye et al. 2023; Kugel et al. 2023), we are well-positioned to refine the current modelling framework. This can be accomplished by replacing certain uninformative or idealised model elements with treatments that are more informed by simulations. During these simulation-based explorations, it is essential to ensure that data selection effects are accurately replicated when constructing mock data from simulations (e.g. Jakobs et al. 2018). We plan to pursue this direction in our future analyses.

5.A Posterior distributions of all free model parameters

In this appendix, we present contour plots displaying the posterior distributions of all free parameters derived from our fiducial model (Sect. 5.4), along with two test models related to the mis-centring parameters (Sect. 5.6.2). We did not show results from the test model with fixed $p_{\rm off} = 1$ due to its lack of convergence. Likewise, we did not include the results from the incompleteness test as it yields constraints almost identical to those of our fiducial model in the same parameters, and the two new incompleteness parameters are not well-constrained.

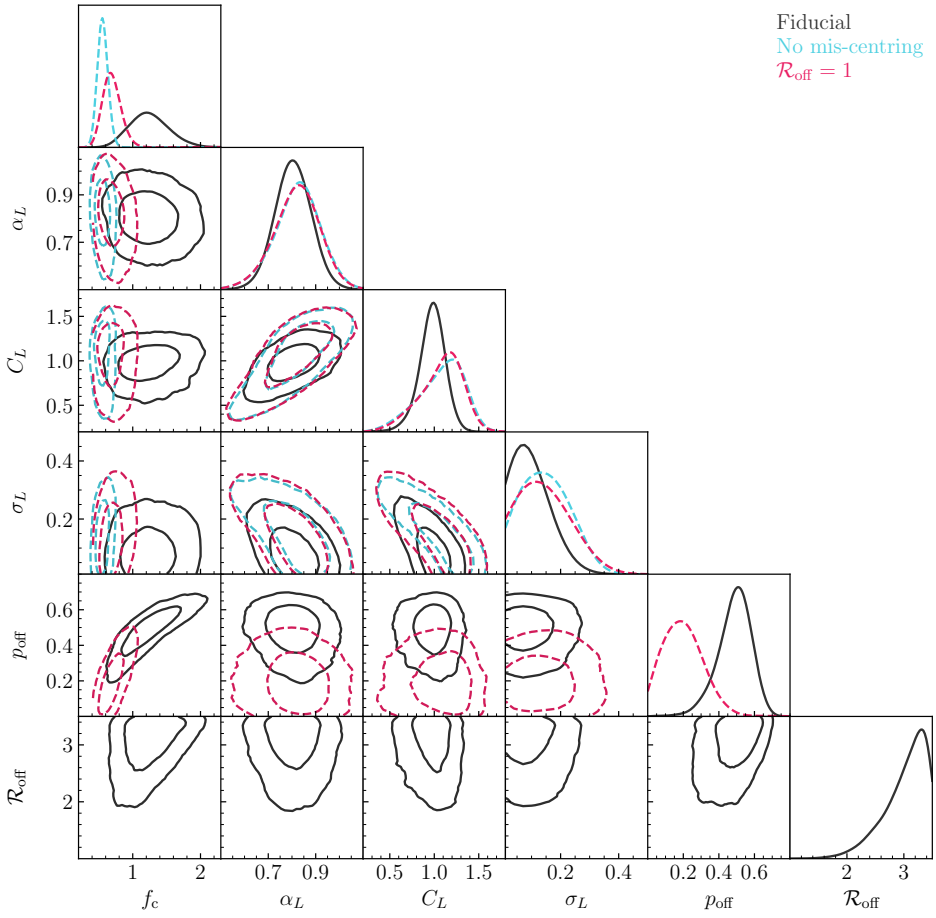

Figure 5.7: Posterior distributions of all free parameters derived from our fiducial model (Sect. 5.4), along with two test models related to the mis-centring parameters (Sect. 5.6.2). The black solid lines signify results from the fiducial six-parameter model, while the magenta and cyan dashed lines represent results from the two mis-centring-related test models. The contours denote the 68% and 95% credible intervals and have been smoothed using a Gaussian kernel density estimation with a bandwidth scaled by a factor of 1. These plots were generated using the ChainConsumer package (Hinton 2016).